Two modes of magnetization switching in a simulated iron nanopillar in an obliquely oriented field

S H Thompson[1,2,3]**, G Brown**[1,4]**, P A Rikvold**[1,3,5] **and M A Novotny**[6,7]

[1] Department of Physics, Florida State University, Tallahassee, FL 32306-4350, USA

[2] Department of Scientific Computing, Florida State University, Tallahassee, FL 32306-4120, USA

[3] Center for Materials Research and Technology, Florida State University, Tallahassee, FL 32306-4350, USA

[4] Center for Nanophase Materials Science, Oak Ridge, TN 37831-6164, USA

[5] National High Magnetic Field Laboratory, Tallahassee, FL 32310-3706, USA

[6] Department of Physics and Astronomy, Mississippi State University, Mississippi State, MS 39762, USA

[7] HPC^2 Center for Computational Sciences, Mississippi State University, Mississippi State, MS 39762, USA

E-mail: hillthompson@gmail.com, gbrown@fsu.edu, prikvold@fsu.edu and man40@ra.msstate.edu

Abstract
Finite-temperature micromagnetics simulations are employed to study the magnetization-switching dynamics driven by a field applied at an angle to the long axis of an iron nanopillar. A bimodal distribution in the switching times is observed, and evidence for two competing modes of magnetization-switching dynamics is presented. For the conditions studied here, temperature $T = 20.2$ K and the reversal field 3260 Oe at an angle of 75° to the long axis, approximately 60% of the switches involve unstable decay (no free-energy barrier) and 40% involve metastable decay (a free-energy barrier is crossed). The latter are indistinguishable from switches that are constrained to start at a metastable free-energy minimum. Competition between unstable and metastable decay may not be confined to the temperature studied in this paper, and could greatly complicate applications involving magnetization switching near the coercive field.

(Some figures in this article are in colour only in the electronic version)

1. Introduction

Nanoscale magnetic devices play important roles in many applications, including sensor technology and magnetic recording. The design process of these devices may rely on micromagnetic simulations that represent such systems with the appropriate resolution, i.e., preserving the actual physical dynamics while maintaining a reasonable simulation effort. This has historically been achieved through the use of semi-classical equations that govern the motion of individual spins on a lattice mapped from a physical magnetic system. In our work, the Landau–Lifshitz–Gilbert (LLG) equation [1]

provides such dynamics for the spins and includes finite-temperature effects by incorporating a stochastic field that obeys a fluctuation-dissipation relation.

Here, a high-resolution model of the magnetization switching of an iron nanopillar is presented. When subjected to a magnetic field of magnitude near the coercive limit, obliquely aligned with respect to the pillar's axis, a bimodal distribution of switching times is observed [2]. This is a feature which may have important ramifications for the application of such nanopillars in real-world devices, which typically rely on a single, consistent decay mode. Other, lower-resolution models of the same physical system also exhibit bimodal switching-

time distributions, however the mechanism leading to this behaviour is different in each model and depends on the resolution of the computational lattice [3]. For the lowest-resolution model, a single macrospin, bimodal switching times are the result of the spin precessing close to the magnetization value that constitutes our definition of a switching event, which sometimes cause switching to occur early due to thermal fluctuations. Bimodal switching times seen in a medium-resolution model, a spin chain, depend on whether one end of the pillar switches or both ends switch at the same time. Trials that involve both ends switching have a change in total magnetization that occurs roughly twice as fast as those with only one end switching. Consequently, lower switching times are observed for switching that happens at both ends concurrently. Further results for the low- and intermediate-resolution models are reported in [3].

Simulations in this paper are performed only for our high-resolution model with a spatial discretization of the order of the exchange length, which enables magnetization configurations that are nonuniform in all three directions of the pillar. The complex magnetization dynamics of this highest-resolution model, discussed in the present paper, preclude a simple description of the mechanism leading to bimodal switching times. This is additionally complicated by the large computational resources needed to generate an adequate statistical picture of the behaviour across a large parameter range. Instead, the high-resolution model is explored here at a specific applied field while generating a large amount of statistics in order to probe the switching mechanism in greater detail. The validity of this approach lies in the fact that, for each of the lower-resolution models, the mechanism leading to bimodal switching times is the same across a large range of the applied field space.

For a bimodal switching-time distribution, the traditional picture of a single free-energy barrier which must be crossed, often used to describe the decay of a metastable state, appears to be insufficient. Furthermore, even a more complicated free-energy surface simulated without random noise, i.e. at zero temperature, would not be able to show the two modes of switching demonstrated for these nanomagnets. Therefore, we analyse the bimodal switching behaviour of simulated nanopillars with a high-resolution model at finite temperature using information from temporal phase portraits, and we also apply absorbing Markov-chain techniques [4–9] to transition matrices obtained from the simulations.

The rest of this paper is organized as follows. We first present the computational model and implementation of the LLG equation in section 2. Section 3 is divided into three parts, which collectively discuss results obtained from the simulations. Section 3.1 explores the phase portraits of the energy during switching, while sections 3.2 and 3.3 provide information about the free energy of the system based on analysis of transition matrices and projective dynamics, respectively. Conclusions are presented in section 4.

2. Model and numerical method

The numerical model is motivated by nanopillars fabricated by von Molnár and collaborators [10, 11]. Using scanning-

tunnelling-microscopy-assisted chemical vapour deposition, they constructed elongated iron nanoparticles, each approximately $10 \times 10 \times 150$ nm^3. Their results indicated that the field-driven magnetization switching in these particles at field strengths near the coercive field is initiated by localized nucleation, involving thermal activation over a free-energy barrier [12–15]. This is expected for systems whose dimensions are large enough to support a nonuniform magnetization [16, 17], in contrast to the single coherent rotation mode assumed for smaller particles via the Stoner–Wohlfarth model [18–20].

In order to numerically investigate these nanopillars, a coarse-grained, cubic computational lattice is used, in which each cell represents the net magnetization of the corresponding volume in the physical system. To ensure that the magnetization density is uniform at length scales below the cell volume, the lattice spacing is chosen smaller than the exchange length of 2.6 nm, obtained from the material properties of bulk iron [21]. This criterion yields a regular lattice with the dimensions $6 \times 6 \times 90$ ($N_s = 3240$ spins, $\Delta x = 1.6667$ nm), which has a single classical Heisenberg spin at the centre of each site. The time evolution of this spin, $\vec{m}(\vec{r}_i)$, is controlled by the LLG equation [1, 22, 23],

$$\frac{\mathrm{d}\vec{m}(\vec{r}_i)}{\mathrm{d}t} = -\frac{\gamma_0}{1 + \alpha^2}$$
$$\times \left(\vec{m}(\vec{r}_i) \times \left[\vec{H}(\vec{r}_i) + \frac{\alpha}{m_s}\vec{m}(\vec{r}_i) \times \vec{H}(\vec{r}_i) \right] \right), \qquad (1)$$

which updates every site on the lattice at each computational time step. At each site i, the local field $\vec{H}(\vec{r}_i)$ determines the direction of change of the magnetization $\vec{m}(\vec{r}_i)$ during the next integration step. The parameters $\gamma_0 = 1.76 \times 10^7$ Hz Oe^{-1}, $m_s = 1700$ emu cm^{-3}, and $\alpha = 0.1$ represent the electronic gyromagnetic ratio, the saturation magnetization of bulk iron, and a phenomenological damping parameter, respectively. Values for these parameters are consistent with the material properties of bulk iron, and are discussed in previous work [2, 21, 24]. The total local field, $\vec{H}(\vec{r}_i)$, is a sum of the individual fields, which include the dipole field $\vec{H}^D$, the uniform applied (Zeeman) field $\vec{H}^Z$, and the exchange field $\vec{H}^E$ [21].

Only nearest-neighbour interactions are considered for the exchange field $\vec{H}^E$, while the long-range dipolar interaction, $\vec{H}^D$, couples all computational cells to each other. Consequently, the dipolar term constitutes the largest computational task during an integration step of the simulation, scaling as $O(N_s^2)$ for a brute-force calculation. This term is reduced to a linear dependence on the number of cells, N_s, by using the fast multipole method [21, 25], resulting in simulation rates of approximately 0.041 ns/CPU-hour on a Dual-Core 2220 2.8 GHz Opteron processor with 2 GB RAM per core using the C++ Psimag library [26]. This equates to approximately 26 000 CPU-hours for the 100 trials discussed in the following sections.

The temperature is set to 20.2 K, and is included in the simulation through the stochastic field $\vec{H}^T$, whose components are Gaussian distributed with mean zero and
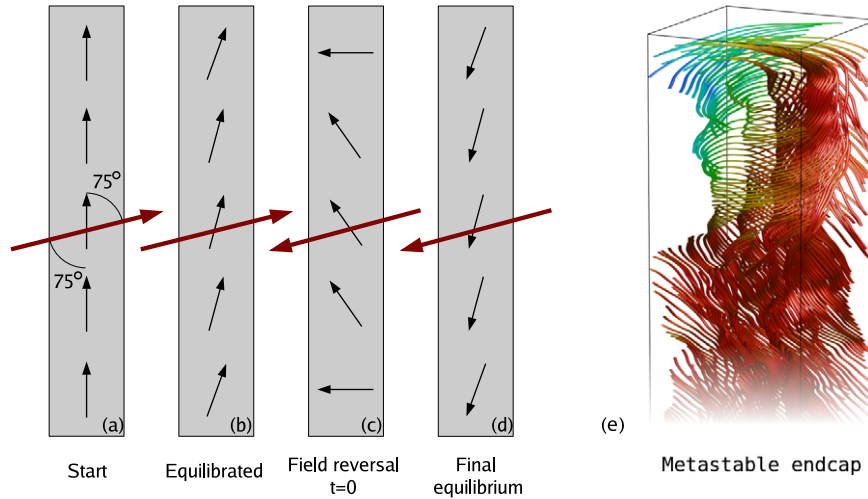
Figure 1. Schematic of pillar magnetization (small arrows, black online) and the uniform applied field (large arrows, red online) at different times during a trial. In these images, the *z*-axis (up–down) has been compressed to about one-third of the original height. (a) Initially, at $t = -0.25$ ns, the magnetization is aligned with the long axis of the pillar and the applied field has a value of 3260 Oe, oriented at 75° with respect to the long axis. (b) Some time later, at $t = -0.125$ ns, the magnetization is relaxed and the applied field begins its sinusoidal reversal as described in section 2. (c) The field reversal is complete at $t = 0$ ns. (d) The final equilibrium of the simulation after magnetization switching has occurred. (e) Snapshot of a pillar endcap while in the metastable state, corresponding to the schematic of (c). Lines in this snapshot trace out the interpolated, continuous magnetization and are colour-coded by m_z. The scale is up (dark grey, or dark red online) to down (light grey, or light blue online). The waviness of the lines indicates the presence of thermally excited spin waves.

variance determined by the fluctuation-dissipation relation,

$$\langle H_\beta^{\mathrm{T}}(\vec{r}_i, t) H_\gamma^{\mathrm{T}}(\vec{r}_j, t') \rangle = \frac{2\alpha k_{\mathrm{B}} T}{\gamma_0 m_{\mathrm{s}} V} \delta_{ij} \delta_{\beta\gamma} \delta(t - t'), \quad (2)$$

where k_{B} is Boltzmann's constant, V is the volume of an individual computational cell, T is the absolute temperature, δ_{ij} and $\delta_{\beta\gamma}$ are Kronecker deltas over the lattice sites i, j and directions β, γ, respectively, and $\delta(t - t')$ is a Dirac delta function of the time difference, $t - t'$. This equation implies that the magnitude of the thermal field scales linearly with the square root of the temperature. The details of the integration of the stochastic field are discussed in [21].

The simulation begins with the pillar in an applied field of magnitude 3260 Oe and angle 75° with respect to the long axis of the pillar (figure 1(a)). Once equilibrated, most of the spins are relaxed in the direction of the initial applied field (figure 1(b)). The value of the applied field is then changed sinusoidally over a time period of $t = 0.125$ ns and is finally anti-parallel to the initial field, i.e., $\vec{H}^Z(t) = \vec{H}_0^Z \cos(\pi t / 0.125 \text{ ns})$ with $t \in [-0.125 \text{ ns}, 0]$. For $t > 0$, $\vec{H}^Z(t) = \vec{H}_0^Z$ and remains constant with a negative *z*-component (figure 1(c)). This field reversal protocol prevents the Zeeman energy from excessively exciting the system. Also shown in figure 1 is the typical high-curl magnetization configuration of the endcap (e), which occurs after the field reversal (c), but before switching occurs.

3. Numerical results

Under the conditions described in section 2, $N = 100$ magnetization-switching simulations were performed. The switching-time t_{s} is defined as the first-passage time

to the *z*-component of the total magnetization $M_z = (1/(N_{\mathrm{s}} m_{\mathrm{s}})) \sum_i m_z(\vec{r}_i) \leqslant 0$, with time measured from the completion of the field reversal. From these 100 trials, the cumulative distribution of the switching times, shown in figure 2(a), indicates at least two characteristic timescales and the existence of more than a single switching path. About 60% of the simulations (59 runs) switched almost immediately ($t_{\mathrm{s}} < 2.1$ ns), while the remaining 40% (41 runs) exhibited switching times $t_{\mathrm{s}} > 2.5$ ns and up to an order of magnitude larger. Since direct comparison of the magnetization of individual runs did not reveal any obvious differences in the switching mechanism, the trials are divided into two groups based only on the location of the sharp corner of the cumulative switching probability in figure 2(a). Located near the probability 0.6, this corner provides a clear distinction between two characteristic groups of switching times in the distribution. These two groups are labelled as 'fast' decay ($t_{\mathrm{s}} < 2.5$ ns) and 'slow' decay ($t_{\mathrm{s}} \geqslant 2.5$ ns). Below we show that the slow-mode statistics are the result of a process which must traverse a free-energy landscape characterized by a metastable well that the system must escape to reach the lowest available free-energy state. This is accomplished by the collective effect of many random thermal fluctuations that eventually cause the system to surmount the free-energy saddle point that separates the metastable well from the global free-energy minimum. The fast-mode statistics, however, reveal a switching path in the free energy that completely avoids the metastable well, as will be shown in sections 3.2 and 3.3.

Based on the shape of the cumulative distribution for each mode (figure 2), an exponential form is assigned to fit the switching-time probability density function (pdf). To find the lifetime, τ, of each mode, the mean switching-time, $\langle t_{\mathrm{s}} \rangle = (1/N) \sum_i t_{\mathrm{s}_i}$, and the standard deviation,
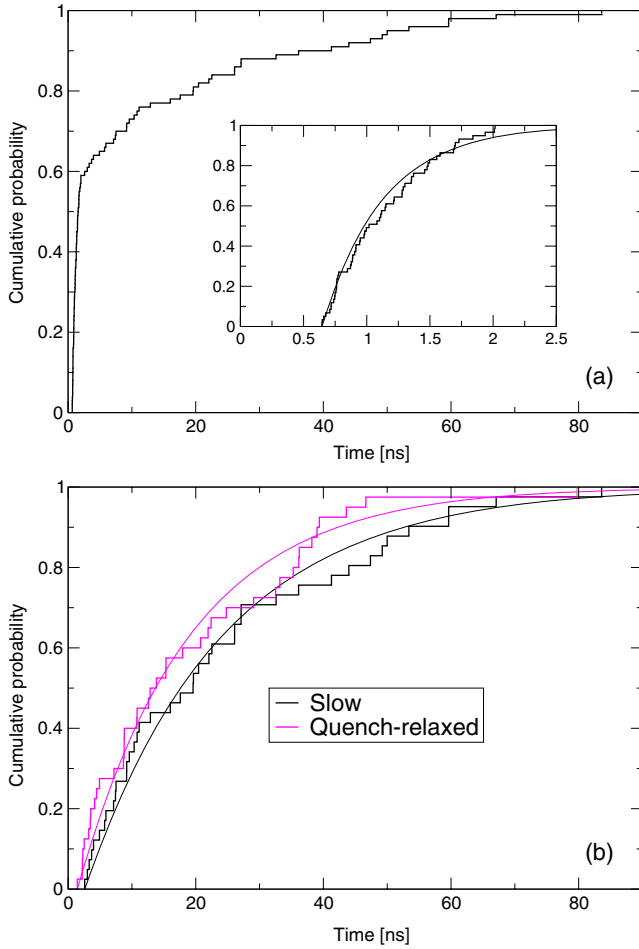
Figure 2. Cumulative switching-time distribution for all 100 full runs, with only the fast mode shown as an inset (a) and a comparison of quenched-relaxed and slow runs (b). It is clear from (a) that at least two characteristic timescales are present in the switching statistics for this system. From the measured lifetimes of the trials, the maximum-likelihood estimate for the lifetime, τ, is $\tau = 0.5$ ns for the fast mode (59 trials), $\tau = 21.7$ ns for the slow mode (41 trials), and $\tau = 17.7$ ns for the QR trials (40 trials). See table 1 for a summary of the lifetime measurement results. The fitted expressions, $D(t) = \eta(t - t_0)(1 - \exp(-(t - t_0)/\tau))$, where η is the Heaviside step function, are also shown for the separated sets of data.

$\sigma_{\mathrm{s}} = \sqrt{(1/(N - 1)) \sum_i (t_{s_i} - \langle t_{\mathrm{s}} \rangle)^2}$, are determined from the empirical data. The delayed exponential, $f(t) = \eta(t - t_0)(1/\tau) \exp(-(t - t_0)/\tau)$, where η is the Heaviside step function and $t_0 = \min[\min\{t_{s_i}\}, \langle t_{\mathrm{s}} \rangle - \sigma_{\mathrm{s}}]$, is used as the pdf. We found good agreement between the fitted expression and the empirical data with a corresponding one-sided Kolmogorov rejection probability [27] of 0.12 and 0.07 for the slow and fast modes, respectively. Once the delay time t_0 was determined, our estimate for the lifetime was found as $\tau = \langle t_{\mathrm{s}} \rangle - t_0$. The slow-mode lifetime from this estimate is $\tau = 21.7$ ns, with a corresponding $t_0 = 2.6$ ns. The results for the slow-mode switches are shown in figure 2(b) and table 1, with τ for the slow mode close to other estimates that will be discussed below. In comparison, the lifetime for the fast mode is $\tau = 0.5$ ns, with $t_0 = 0.6$ ns.

In addition to the above switches, 40 separate simulations were also completed under conditions identical to the previous

Table 1. Lifetimes were obtained by the following methods: $\langle t_{\mathrm{s}} \rangle$ is the empirical mean obtained from the switching times of the actual simulations, and σ_{s} is the corresponding standard deviation. For the slow and QR modes, characterized by the pdf $f(t) = \eta(t - t_0)(1/\tau) \exp(-(t - t_0)/\tau)$, t_0 is found from $\min[\min\{t_{s_i}\}, \langle t_{\mathrm{s}} \rangle - \sigma_{\mathrm{s}}]$, and $\tau = \langle t_{\mathrm{s}} \rangle - t_0$. τ_{EV} is obtained from the eigenvalues of the transition matrix (section 3.2). τ_{RT} is found from the residence times of the projective dynamics (PD) analysis (section 3.3).

	Fast mode (ns)	Slow mode (ns)	QR (ns)
$\langle t_{\mathrm{s}} \rangle$	1.1	24.3	19.1
t_0	0.6	2.6	1.4
σ_{s}	0.4	20.7	17.0
τ	0.5	21.7	17.7
τ_{EV}	0.2	22.8	17.9
τ_{RT}	1.3	24.8	19.7

ones except for the details of the initial magnetization and field reversal. The initial magnetization of these runs was determined by quenching one slow-mode configuration to 0 K while in the metastable well, without changing the field. The new simulation began by rethermalizing, again setting the temperature to 20.2 K. From this time on ($t = 0$), the simulations were carried out identically to the previous 100 trials. We call this the quenched-relaxed procedure (QR). The reasons for adopting it are explained in section 3.1. Along with the slow mode, the cumulative distribution of lifetimes for these QR runs is shown in figure 2(b), with $\tau = 17.7$ ns, $\sigma_{\mathrm{s}} = 17.0$ ns, and $t_0 = 1.4$ ns used for the delayed exponential and a corresponding one-sided Kolmogorov rejection probability of 0.18.

3.1. Phase portraits

Phase plots of the energy also provide information about the behaviour of the simulated nanopillar system. Such plots are shown in figure 3, with the energies due to dipolar and Zeeman contributions on separate axes. The collection of all runs belonging to a particular mode are shown in the background of each plot, with a single run overlaid on top. For the fast (a) and slow (b) modes, the simulations begin near the top of the plots, where the density of points is low. During the initial relaxation of these simulations, both modes evolve down and to the right (i.e., decrease in Zeeman energy E^{Z} (also a decrease in $M_z \in [-1, 1]$, the z-component of the total magnetization) and increase in dipolar energy). The obvious difference between plots (a) and (b) is the path that each takes near the metastable well ($E^{\mathrm{Z}} \approx -1240$ erg cm^{-3}, $M_z \approx 0.72$) and saddle point ($E^{\mathrm{Z}} \approx -1450$ erg cm^{-3}, $M_z \approx 0.66$), determined by projective dynamics in section 3.3. The slow-mode trajectories proceed to the metastable well which can be seen in plot (b) as the large dark region in the centre of the plot. For the slow mode, the simulation spends most of its time here. However, the fast-mode events ignore this attractor almost completely, mostly slowing down only near the saddle point. This is not unreasonable, since the free energy near the saddle point necessarily has a small gradient, and the driving force is therefore weak. Both modes continue the switching process toward the global free-energy minimum located below
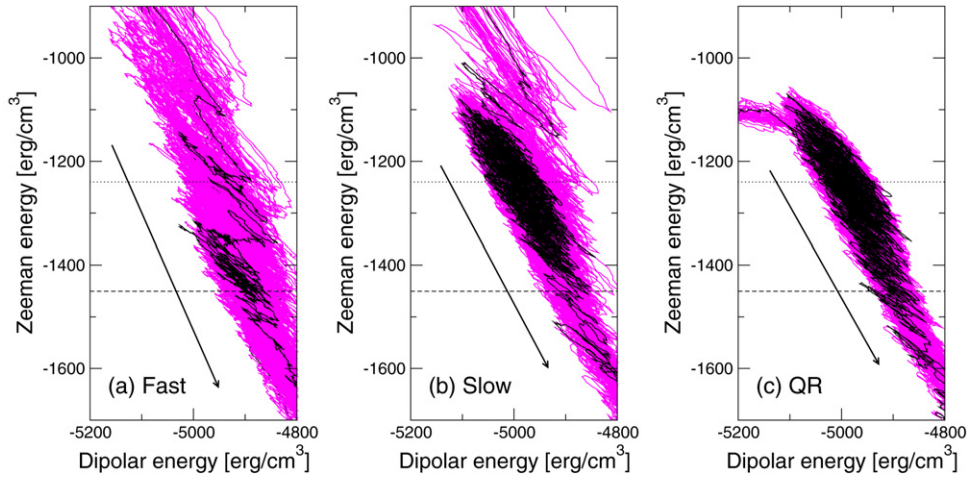
Figure 3. Phase plots in the space of dipolar and Zeeman energies for 59 runs belonging to the fast mode (a), 41 runs belonging to the slow mode (b), and 40 runs belonging to the quenched-relaxed trials (c). The lighter background (red online) is the collection of all runs belonging to a particular mode, while the darker path (black) represents a single run. Also shown on the E^Z axis is the location of the metastable well (horizontal dotted line) and saddle point (horizontal dashed line), determined in sections 3.2 and 3.3. Arrows indicate the average direction of motion of the phase portrait.

the displayed portion of the phase portraits. These results suggest that the difference between the fast and slow modes is the visitation of the metastable well by the slow mode. This is further supported by the QR simulations.

To investigate the properties of the metastable free-energy well, several randomly chosen trials from the 100 simulations were quenched and rethermalized to force metastable behaviour. Quenches initiated at values of E^Z higher than the saddle point (≈ -1450 erg cm^{-3}) equilibrated to a common $T = 0$ K metastable configuration located more negative than $E^D \approx -5200$ erg cm^{-3} along the dipolar axis of figure 3(c) (not visible), representing the common initial configuration for all QR trials. This $T = 0$ K configuration was consistently reached by all chosen trials belonging to both the slow and fast modes and from various values of $E^Z >$ -1450 erg cm^{-3} during the switching process. The resulting initial configuration quickly proceeds to the $T = 20.2$ K metastable well when thermalized. Other quenches, which were initiated at values of E^Z below the saddle point, settled into configurations near the $T = 20.2$ K final absorbing state and were not used in the QR trials.

Since the QR simulations necessarily start in the metastable well, they do not have the same behaviour as the fast and slow modes during the rethermalization. They also omit the configurations $E^Z > -1100$ erg cm^{-3} which occur at early times for the slow and fast modes. However, ignoring this initial relaxation, they produce phase plots that closely resemble those for the slow mode. The similarity of the phase plots suggests the QR simulations and the slow mode may also share other features, which are explored in the next subsections.

Also interesting is the large change with T in the phase space location of the metastable state in the QR simulations upon rethermalization. It indicates that the entropy S, which enters the free energy F as $F = E - TS$, has a large influence on the free energy of the system. This observation is further
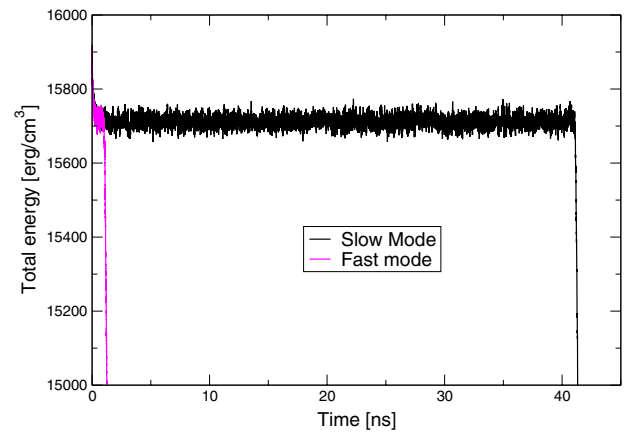

Figure 4. Total energy E as a function of time for a single run belonging to the slow mode and a single run belonging to the fast mode. Near $t = 0$, the total energy quickly decreases as the system initially relaxes. After this, the average value of the total energy remains constant, except for small fluctuations, until the saddle point is crossed.

seen in figure 4, which plots the total energy E of the system as a function of time. Ignoring the fast relaxation following the field reversal, E is nearly the same for both fast and slow modes, remaining constant (except for small fluctuations) until the saddle point is crossed. Since the total energy is nearly the same for both modes, entropy must largely account for the differences in behaviour that define the slow or fast relaxation.

3.2. Transition matrix

Although the phase space in these simulations is very large ($2N_s$ dimensions), it appears from the phase plots in figure 3 that the evolution of the system along the Zeeman energy coordinate, E^Z, can approximately describe the process of magnetization switching. To investigate the possibility of

a one-dimensional description of the switching process, this coordinate was discretized into 400 equal-sized bins for the transition matrix analysis of this section. Individual bins are labelled by the index $i = 1, \ldots, k$. We found the results of this section to be approximately independent of the axis discretization, and we therefore use 400 bins since it provides numerically stable results for all of the Markov-chain techniques of this section. Each measurement of E^Z during the simulation corresponds to a particular bin i, and this discretized state can be represented by a unit vector $\langle \hat{i} |$ consisting of one in the ith position with all other elements equal to zero.

The matrix, $\mathbf{M}$, of transition probabilities between states is also constructed by sampling the series of E^Z values during the simulation. Individual elements of the transition matrix, M_{ij}, are obtained by enumerating the single transitions from bin j to bin i corresponding to a time step, $\Delta t \approx 3.3 \times 10^{-4}$ ns, equal to the measurement interval during the simulations, and normalizing such that $\sum_j M_{ij} = 1$. Thus, the probability of going from $\langle \hat{i} |$ to $\langle \hat{j} |$ in one time step is given by the matrix element M_{ij} with the result that,

$$\langle u(t + \Delta t) | = \langle u(t) | \mathbf{M}, \tag{3}$$

where $\langle u(t) | = \sum_i \langle u(t) | \hat{i} \rangle \langle \hat{i} | = \sum_i p_i(t) \langle \hat{i} |$ is the row vector representing the probability that E^Z is in bin i at time t. Therefore, $\mathbf{M}$ provides the average change in the state of the system after one time step [4]. These transition probabilities are estimated by combining statistics from all individual runs belonging to a particular mode (fast, slow, or QR).

Since on average the time evolution of the simulation decreases E^Z, the system begins in state $\langle \hat{k} |$ and ends when the absorbing state $\langle \hat{1} |$ is reached and $M_z \leqslant 0$ (the z-component of the total magnetization is $\leqslant 0$). From this condition, the matrix element $M_{11} = 1$ signifies this absorbing state. The transition matrix representing this absorbing Markov-chain thus has the form [5],

$$\mathbf{M}_{(r+s)\times(r+s)} = \begin{pmatrix} \mathbf{I}_{r\times r} & \mathbf{0}_{r\times s} \\ \mathbf{R}_{s\times r} & \mathbf{T}_{s\times s} \end{pmatrix}. \tag{4}$$

Here, $\mathbf{I}$ is an identity matrix which, in general, represents r absorbing states (here, $r = 1$). $\mathbf{R}$ is the recurrent matrix, which describes the probability of moving into the absorbing state from any other state, $\mathbf{0}$ is a null matrix, and $\mathbf{T}$ is the transient matrix, which describes the evolution of the system before absorption.

By this construction, $\mathbf{M}$ is a non-symmetric, regular, non-negative square matrix with row sums equal to one and with different left and right eigenspaces. The Perron–Frobenius theorem [5] provides a general property for this type of matrix, namely that there exists a unique eigenvalue of $\mathbf{M}$ equal to unity, which is larger than the magnitudes of all other eigenvalues of $\mathbf{M}$. For our matrix, the left eigenvector associated with the largest eigenvalue of $\mathbf{M}$ is $\langle \lambda_1 | = \langle \hat{1} | = (1, 0, 0, \ldots, 0)$. This represents the probability distribution characterizing the absorbing state.

The other eigenvalues of $\mathbf{M}$ correspond to decaying deviations from the equilibrium distribution since $\langle \lambda_1 | \mathbf{M} = \langle \lambda_1 |$ and

$$\langle \lambda_\alpha | \mathbf{M} = \lambda_\alpha \langle \lambda_\alpha | \tag{5}$$
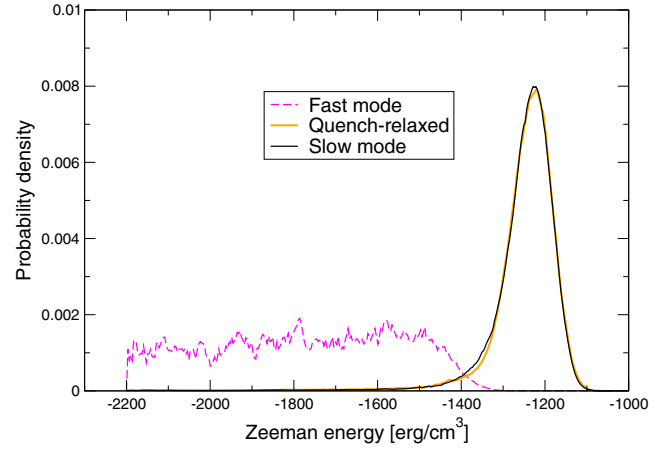

Figure 5. Probability distributions obtained from the eigenvectors corresponding to the second largest eigenvalue for the fast and slow modes and the QR simulations. In this figure, the Zeeman axis has been discretized into 400 bins. We found the probability densities to be approximately independent of the discretization. These distributions are constructed from all the data belonging to each mode, as discussed in section 3.2. The slow and QR distributions have a well-defined peak at the location of the metastable free-energy well, with the QR distribution almost hidden behind the slow-mode result. The fast mode, however, is quite wide with an approximately uniform probability density below the free-energy saddle point in the Zeeman energy (see section 3.3), and close to zero above. The cutoff, $M_z = 0$, corresponds to $E^Z \approx -2200$ erg cm^{-3}.

with $0 < |\lambda_\alpha| < 1$. Here $\langle \lambda_1 | = \langle \hat{1} |$ denotes the dominant left eigenvector of $\mathbf{M}$, and $\langle \lambda_\alpha |$ is any other left eigenvector of $\mathbf{M}$ with eigenvalue λ_α. As a consequence of the above, the weights of all left eigenvectors of $\mathbf{M}$ except $\langle \lambda_1 |$ will decay to zero under repeated applications of $\mathbf{M}$ since $\langle \lambda_\alpha | \mathbf{M}^n = \lambda_\alpha^n \langle \lambda_\alpha |$. Equations (3) and (5) together are used to find the lifetime τ of the αth eigenstate, with the result that,

$$\langle \lambda_\alpha(t) | = \lambda_\alpha^t \langle \lambda_\alpha(0) | \approx e^{-(1-\lambda_\alpha)t} \langle \lambda_\alpha(0) |. \tag{6}$$

Since $\langle \lambda_2 |$ corresponds to the second longest-lived state of the system, $\tau_{EV} = 1/(1-\lambda_2)$ approximates the average lifetime of the metastable state of the system in units of the measurement time resolution, Δt.

A probability distribution representing the metastable state can be built from a properly normalized linear combination of $\langle \lambda_1 |$ and $\langle \lambda_2 |$, $\langle \text{meta} | = \langle \lambda_1 | + b \langle \lambda_2 |$, with λ_2 well separated from λ_3. Here, the scaling constant b constrains the resulting vector to have zero weight in the absorbing state and ensures that the probability is normalized ($\sum_i \langle \text{meta} | \hat{i} \rangle = 1$). As can be seen in figure 5, the slow and QR metastable state probability distributions found using this method have a similar shape and exhibit peaks revealing the location of the metastable free-energy well. The location of these peaks agree with the phase portrait results of section 3.1 for the longer-lived trials and clearly pinpoint the free-energy minimum along the Zeeman axis. The fast mode, however, does not have a dominant peak in the probability distribution that might be expected based on the phase portraits. Rather, the probability density is close to zero near the metastable free-energy well and spread out along the remainder of the axis.

This may indicate the sub-dominant eigenvalue is not well separated from the rest of the eigenvalue spectrum and that the probability densities associated with these shorter transients are also important. Nevertheless, these results reinforce the conclusion that the fast-mode switches simply do not fall into the metastable well.

3.3. Projective dynamics

The transition matrix of section 3.2 accounts for all transitions that may occur from a given bin, potentially with all elements of the submatrices **R** and **T** non-zero. However, if the bin sizes are chosen sufficiently large, the matrix becomes tridiagonal. To satisfy this condition, 200 equal-sized bins are used and the one-dimensional description of the magnetization switching becomes a one-step Markov process [4]. Using this single, coarse-grained variable, the projective dynamics (PD) method [4, 6–9] can be used to measure the growth probabilities P_G and shrinkage probabilities P_S of the stable phase along this coordinate. Once obtained, several properties of the projected free energy $F(E^Z)$ can be measured via P_G and P_S. A key advantage of the PD technique is that it provides information about the location of the saddle point in the free energy. This is generally a difficult feature to extract, as the statistics in this region are usually sparse.

The PD method is implemented as follows. First, the E^Z axis is broken into a number of bins, as described for the transition matrix approach in section 3.2. The bin size is determined such that each time step is only capable of moving the system between adjacent bins, corresponding to discretizing the E^Z axis into 200 bins for the PD analysis. Histograms of $P_G(E^Z)$, $P_S(E^Z)$, and the probability to stay in the same bin, $P_N(E^Z)$, keep a record of the changes along the axis and are updated at each measurement. Once completed, the histogram is normalized so that $P_G(E^Z) + P_S(E^Z) + P_N(E^Z) = 1$.

For the present nanopillar simulations, we attempted to use as the slow (binned) variables the Cartesian components of the total magnetization, as well as other contributions to the total energy. However, the Zeeman energy provided the clearest crossings of the probabilities for the projective dynamics technique. This is reasonable since it provides the closest correspondence to the path observed in figure 3.

Points along E^Z where $P_G = P_S$ define local extrema of the free energy. This is true since $P_G > P_S$ implies $dF/dE^Z > 0$ and $P_S > P_G$ implies $dF/dE^Z < 0$. For our system, which has a single metastable free-energy well, these extrema represent the location of the metastable well, the saddle point, and the true equilibrium in the free energy. The latter is not observed in our simulations due to the cutoff at $M_z \leqslant 0$.

Figures 6(a) and (b) show PD plots for the fast and slow modes, respectively. Each plot contains the data of all the runs belonging to each mode (points), which have then been smoothed using a five-point running average (solid curves). The location of the metastable free-energy well for the slow-mode switches (first crossing from the right in figure 6(b), $E^Z \approx -1240$ erg cm^{-3}, $M_z \approx 0.72$) coincides with the peaks
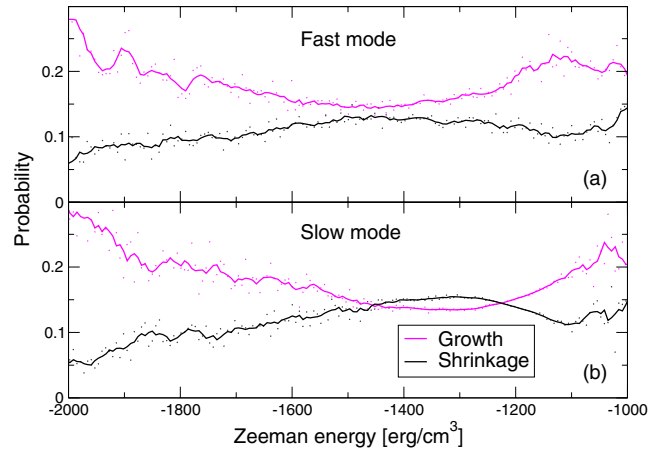

Figure 6. Projective dynamics results for the two modes, fast (a) and slow (b). The slow mode exhibits clear crossings of the growth and shrinkage probabilities, indicating extrema in the free energy, corresponding to the metastable well (right) and the saddle point (left). Conversely, the probabilities for the fast mode only nearly overlap in this same region. The solid curves are five-point running averages.

present in the probability distribution for the longer-lived trials, figure 5, of section 3.2. Further left, the second crossing in figure 6(b) indicates the saddle point in the free energy, which is located at $E^Z \approx -1450$ erg cm^{-3}, $M_z \approx 0.66$. The locations of both the metastable well (first crossing from the right) and the saddle point (second crossing from the right) are obvious for the slow mode. This is expected since the results of section 3.2 indicate true metastable behaviour.

From our data, the lowest growth probability, P_G, for the fast mode occurs around $E^Z = -1450$ erg cm^{-3}, $M_z \approx 0.66$ which is identified as the location of the saddle point in the free energy from the slow-mode statistics. Here, fast switches proceed through a region of the free-energy landscape with a small, but negative slope. Along with the results of the probability distributions, this indicates the absence of a metastable state in the fast mode. These results agree with the probability distributions (figure 5) obtained from the transition matrices of section 3.2, as well as provide information about the location of the saddle point in the free energy.

The PD results of the quenched-relaxed system can be compared to the slow modes. As seen in figure 7, the QR system and the slow-mode probabilities near the metastable minimum cross at nearly identical values of E^Z. The PD technique reveals that the slow mode and QR trials not only share similar locations of the free-energy metastable well, but also pass through saddle points that look nearly identical in this projected space.

Together, the PD results and the probability distributions imply that, once in the metastable well (the slow and QR decays), the system must be thermally activated to overcome the free-energy saddle point. On the other hand, these results indicate that if the metastable well is avoided (the fast mode), the system only has to traverse a relatively flat free-energy landscape to switch.

Lifetimes can be calculated easily from the results of the PD technique [4] and compared to those obtained from other
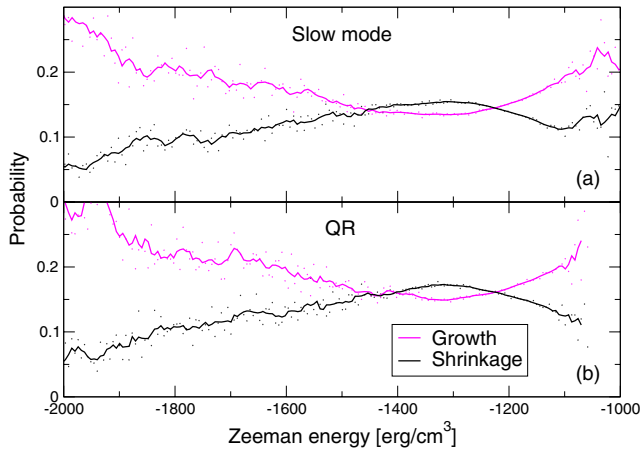
Figure 7. Projective dynamics results for the two modes, slow and quenched-relaxed (QR). It is easy to see that these simulations share the same statistical behaviour in this region, including nearly identical crossing values (which are locations of the extrema of the free energy). As with figure 6, the solid lines represent five-point running averages.

techniques used in this paper. The residence time for each bin, $h(i)$, is defined as the average time spent in state i. In addition, $P_G(i)h(i)$ is the average number of times the system moves from state i to $i-1$ (the absorbing state is state one). If the system is to reach the absorbing state exactly once, then

$$P_G(i)h(i) - P_S(i-1)h(i-1) = 1 \qquad (7)$$

must be true. Since the absorbing state has zero shrinkage probability, $P_S(1) = 0$, the residence time of the previous state can be found by $h(2) = 1/P_G(2)$. This leaves an iterative solution for the remaining states,

$$h(i) = \frac{1 + P_S(i-1)h(i-1)}{P_G(i)}. \qquad (8)$$

Consequently, the average lifetime of the process is the sum of the residence times, $\tau_{RT} = \sum_i h(i)$.

A summary of the lifetimes obtained by all the techniques used in this paper is provided in table 1. We expect some bias in the lifetime data due to the artificial cut made when sorting fast and slow modes. Trials with lifetimes <2.5 ns are considered fast modes, although there is some probability that they may belong to the slow mode, albeit with a short individual lifetime.

Differences between τ_{EV} and the other measurements of the fast-mode lifetimes may be due either to statistical error, which is not included in the transition matrix associated with τ_{EV}, or to the analysis of a single eigenmode not being sufficient for the fast mode. The latter may be particularly important since the eigenvalue spectrum for the fast mode is very closely spaced below the largest eigenvalue. We expect the slow and QR lifetimes obtained from the eigenvalues of the transition matrix to be more robust against this error, due to the larger amount of statistics gathered from longer runs.

Measurements of the QR lifetime yield slightly shorter values than for the slow-mode measurements from the full simulation. This is expected since the QR trials begin close to the bottom of the free-energy metastable well upon rethermalization and consequently do not include relaxation into this area.

In addition, the lifetime measurements obtained from the residence time for all modes show slightly larger values. Since this is a sum of the average time spent in all states for each mode, this method includes the initial t_0, which is subtracted from $\langle t_s \rangle$ to give τ. After considering the biases associated with each measurement technique, the lifetimes agree very well with one another and reinforce the choice of using the Zeeman axis as the projection variable.

4. Conclusions

We have studied the magnetization-switching properties of a simulated iron nanopillar motivated by experimental research [10, 11]. Under the realistic physical conditions described here, we found the presence of more than one characteristic switching-time, which were labelled as 'fast' and 'slow' modes. Through phase portraits and numerical results provided by transition matrices and the projective dynamics method, differences between these two modes were identified. Our results indicate that the fast mode is associated with switching dynamics that do not carry the system through a deep metastable well. This idea is supported by data from separate simulations in which the system was quenched to 0 K while near the metastable well and then rethermalized. These quenched-relaxed simulations also indicate that the entropy provides a large contribution to the free energy of the system. Using transition matrices obtained from the average behaviour of each mode, we also constructed projective dynamics plots and metastable probability distributions which further provide evidence that the fast mode does not encounter a metastable free-energy well and evolves across a relatively flat free-energy landscape. In addition, lifetimes were obtained by measurement, by fitting to the cumulative distribution, by sub-dominant eigenvalues, and by residence times from projective dynamics as reported in table 1. Lifetime values also help to ensure that an appropriate axis was chosen to project the dynamics of the system onto for the analysis of sections 3.2 and 3.3.

We have extended the scope of these results in other work [3] by comparing bimodal switching behaviours of models with lower lattice resolutions. The results suggest bimodal switching-time distributions at the lower resolutions are caused by different mechanisms. The present high-resolution results predict multiple switching mechanisms that rely on nonuniform transverse magnetization that may exist in physical nanopillars and are not seen in the lower-resolution models. These results may be verified experimentally and may have important ramifications for technological applications that rely on a single, consistent switching mode, such as memory devices.

References

[1] Brown W F 1979 *IEEE Trans. Magn.* **15** 1196
[2] Thompson S H, Brown G and Rikvold P A 2005 *J. Appl. Phys.* **97** 10E520
[3] Thompson S H, Brown G, Kuhnle A D, Rikvold P A and Novotny M A 2009 *Phys. Rev. B* **79** 024429
[4] Novotny M A 2001 *Annual Reviews of Computational Physics* vol IX, ed D Stauffer (Singapore: World Scientific) pp 153–210
[5] Iosifescu M 1980 *Finite Markov Processes and their Applications* (New York: Wiley)
[6] Kolesik M, Novotny M A and Rikvold P A 1998 *Phys. Rev. Lett.* **80** 3384
[7] Kolesik M, Novotny M A, Rikvold P A and Townsley D M 1998 *Computer Simulation Studies in Condensed-Matter Physics* vol X, ed D P Landau *et al* (Berlin: Springer) pp 246–51
[8] Brown G, Novotny M A and Rikvold P A 2004 *Physica* B **343** 195
[9] Kolesik M, Novotny M A and Rikvold P A 2003 *Int. J. Mod. Phys.* C **14** 121
[10] Kent A D, Shaw T M, von Molnár S and Awschalom D D 1993 *Science* **262** 1249
[11] Wirth S, Field M, Awschalom D D and von Molnár S 1998 *Phys. Rev. B* **57** R14 028
[12] Wirth S and von Molnár S 2006 *Handbook of Advanced Magnetic Materials* (*Nanostructural Effects* vol 1) ed Y Liu *et al* (New York: Springer) pp 294–338
[13] Li Y, Xiong P, von Molnár S, Ohno Y and Ohno H 2005 *Phys. Rev. B* **71** 214425
[14] Wirth S, Anane A and von Molnár S 2000 *Phys. Rev. B* **63** 012402
[15] Li Y, Xiong P, Wirth S, Ohno Y, Ohno H and von Molnár S 2002 *Appl. Phys. Lett.* **80** 4644
[16] Weiser R, Nowak U and Usadel K D 2005 *Phys. Rev. B* **69** 064401
[17] Hertel R and Kirschner J 2004 *Physica* B **343** 206
[18] Stoner E C and Wohlfarth E P 1948 *Phil. Trans. R. Soc.* A **240** 599
[19] Bonet E, Wernsdorfer W, Barbara B, Benoît A, Mailly D and Thiaville A 1999 *Phys. Rev. Lett.* **83** 4188
[20] Jamet M, Wernsdorfer W, Thirion C, Dupuis V, Méinon P, Pérez A and Mailly D 2004 *Phys. Rev. B* **69** 024401
[21] Brown G, Novotny M A and Rikvold P A 2001 *Phys. Rev. B* **64** 134422
[22] Aharoni A 2000 *Introduction to the Theory of Ferromagnetism* (New York: Oxford University Press)
[23] Brown W F 1963 *Micromagnetics* (New York: Wiley)
[24] Thompson S H, Brown G and Rikvold P A 2005 *Computer Simulation Studies in Condensed-Matter Physics* vol XVII, ed D P Landau *et al* (Berlin: Springer) pp 196–200
[25] Greengard L F 1988 *The Rapid Evaluation of Potential Fields in Particle Systems* (Cambridge, MA: MIT Press)
[26] http://psimag.org/
[27] Press W, Teukolsky S, Vetterling W and Flannery B 1996 *Numerical Recipes in Fortran 77* (New York: Cambridge University Press)